Article

Far Wake and Its Relation to Aerodynamic Efficiency

Sidaard Gunasekaran [1,*,†] **and Aaron Altman** [2,†]

1   Department of Mechanical and Aerospace Engineering, University of Dayton, 300 College Park, Dayton, OH 45469, USA
2   Air Force Research Labs, Dayton, OH 45433, USA; aeroaltman@gmail.com
*   Correspondence: gunasekarans1@udayton.edu
†   These authors contributed equally to this work.

Abstract: Correlations were found between the aerodynamic efficiency and the mean and fluctuating quantities in the far wake of a wall-to-wall SD7003 model and an AR 4 flat plate. This correlation was described algebraically by modeling the wake signature as a function of wing geometry and initial conditions. The model was benchmarked against experimental results to elicit the wing performance as a function of angle of attack by interrogating the wake. In these algebraic models, the drag coefficient along with other initial conditions of the turbulent generator (either airfoil or wing) were used to reconstruct the Reynolds Stress distribution and the momentum deficit distribution in the turbulent wake. Experiments were undertaken at the United States Air Force Research Labs Horizontal Free Surface Water Tunnel (AFRL/HFWT). These experiments build on previous results obtained at the University of Dayton Low Speed Wind Tunnel (UD-LSWT) on a cylinder, an AR 7 SD7062 wing, and a small remote control twin motor aircraft. The Reynolds stress and the momentum deficit of the turbulent generators were experimentally determined using Particle Image Velocimetry (PIV) with a minimum of 1000 image pairs averaged at each condition. The variation of an empirical factor (γ) used to match the Reynolds stress and momentum deficit distributions showed striking correlation to the variation of drag and aerodynamic efficiency of the turbulent generator. This correlation suggests that the wing performance information is preserved in the free shear layer 10 chord lengths downstream of the trailing edge (TE) of the wing irrespective of the dimensionality of the flow.

Keywords: wing performance; self preserved wake; turbulence; wake stratification

1. Introduction

Early literature on turbulent flows indicates that the wake flows achieve a self-preserved state (where turbulence production equals turbulence dissipation) where the information about the geometry of the model is lost. Wygnanski, Champagne, and Marasli [1] were the first to challenge the belief that the 'turbulence forgets its origins'. In 1956, Townsend [2] used a velocity scale U_0 and a length scale L_0 (wake-half width) to normalize the mean velocity and the Reynolds stress profiles in the free shear layer wake of a turbulent generator. By normalizing in this manner, it was theorized that the mean velocity and Reynolds stress of the free shear layer were independent of the geometry of the turbulent generators and downstream distance. To verify Townsend's results, Wygnanski, Champagne, and Marasli (mid-1970s) conducted the same experiments and found that the properties in the wake of different turbulent generators are unique, which contradicted Townsend's results. This is because Wygnanski et al. used the momentum thickness θ as the normalizing length scale instead of L_0 used by Townsend. Using conservation of momentum, the momentum thickness of the generator can be estimated directly from the drag coefficient of the turbulent generator through Equation (1).

$$C_D d = 2\theta \tag{1}$$

where C_D is the drag coefficient of the turbulent generator and d is the diameter of the turbulent generator. During their experiments, Wygnanski et al. constructed multiple turbulent wake generators (cylinders, screens, solid strip, flat plate, and symmetrical airfoil) to obtain the same momentum thickness for each. By using momentum thickness as a normalizing length scale, the experiments showed a difference in downstream wake turbulence properties resultant from initial conditions (such as drag coefficient of the turbulent generator C_D).

Additional research performed by William George [3] in the late 1980s confirmed Wygnanski et al.'s results. In 1992, George and Gibson [4] showed that the self-similarity can be observed in the equations governing homogenous shear flows. In addition, they verified that, in these self-preserved flows, the ratio of turbulent energy production rate to its dissipation rate remains constant. They also showed that, when normalized by Reynolds stress and Taylor microscale, the energy spectra scale over all wave numbers have shapes determined by the initial conditions. In a turbulent flow, if the rate of turbulence production is equal to the rate of dissipation, then the turbulence Reynolds number R_l is constant. George and Gibson [4] discovered that every turbulent generator has a unique energy and dissipation spectrum and does not forget its origins on the scales investigated. Because of the unique nature of the wake for each turbulent generator and their dependence on the initial conditions, the hypothesis for the current research was that the performance information from the wing may also be preserved in the wake as well. Hence, the objective of the current research is to investigate the existing relationships and trends, if any, between the far wake properties and the aerodynamic efficiency of the wing.

2. Algebraic Models

Two different models were used to describe the turbulence signature of the wake—a momentum deficit model and a Reynolds stress model. The momentum deficit model describes the mean velocity of the turbulent flow, while the Reynolds stress model describes the Reynolds stress (the product of the fluctuating velocities) in the turbulent flow.

2.1. The Momentum Deficit Model

This model is based on conservation of momentum. By using Newton's second law, any loss in momentum of the freestream should be equal to the drag of the object assuming steady, inviscid, no body force, equal inlet and outlet pressures, no internal pressure variations, and no flow crossing the side boundaries. An example of the velocity profile $U(y)$ behind an object is shown in Figure 1. In this figure, the velocity profile is Gaussian in shape. U_∞ represents the freestream velocity of the flow. The amplitude of the velocity profile (also representing the mean velocity of the velocity profile) is given by the variable U_0. Finally, the wake half width, defined by the value of 99% of U_∞, is given by the variable L_0.
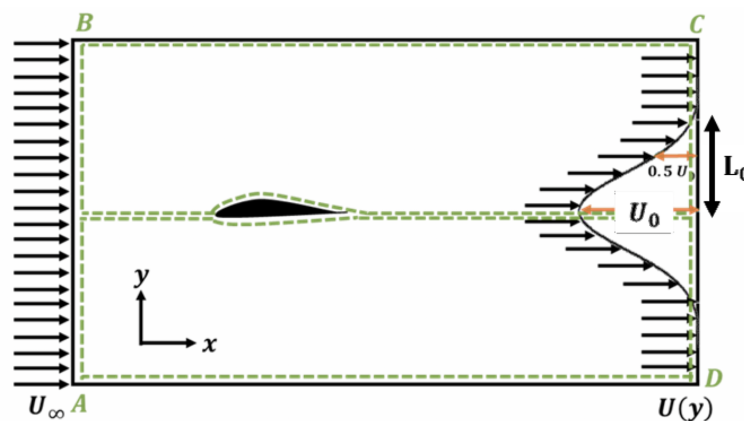

Figure 1. Sketch defining the nomenclature of the momentum wake in turbulent flow.

Assuming inviscid flow, the three-dimensional Euler momentum equation is,

$$\iiint \frac{\partial(\rho\bar{V})}{\partial t}d\forall + \iint (\rho\bar{V}.dA)\bar{V} = -\iiint \nabla P\forall + \iiint (bd\forall) \qquad (2)$$

The first term on the right-hand side of Equation (2) is the pressure term and the second term on the right-hand side of the equations is the body force term. Assuming a one-dimensional flow in the streamwise (x) direction (Figure 2) into and out of the control volume, the Euler equation reduces to,

$$\iiint \frac{\partial(\rho U)}{\partial t}d\forall + \iint (\rho U dA)U = -\iiint (\frac{\partial p}{\partial x})d\forall = M \qquad (3)$$

where M represents momentum of the freestream lost. Assuming incompressible, steady flow with no pressure or body forces, Equation (3) reduces to,

$$\rho \iint (UdA)U = M \qquad (4)$$

On application of the integral to the control volume and assuming that the U velocity in the x-direction is significantly greater than the V velocity in the transverse (y) direction, the momentum of the freestream lost, M, per unit volume due to the presence of the turbulent generator is given by,

$$M = \rho U(y) \int_C^D (U(y) - U_\infty)dy \qquad (5)$$

Equation (5) is also called the momentum deficit principle. Since the wake itself does not have any momentum of its own, according to conservation of momentum, the loss in momentum of the freestream in the wake (M) can be associated with the boundary layer and separation from the turbulent generator where the viscous interaction between the fluid and the surface of the object reduces the momentum of the freestream. The loss in the momentum of the freestream (which is also the drag of the turbulent generator) is given by,

$$D = \rho U_\infty^2 \theta \qquad (6)$$

where θ is the momentum thickness at the trailing edge of the wing. The drag of the turbulent generator is also given by,

$$D = \frac{1}{2}\rho U_\infty^2 dC_D \qquad (7)$$

Setting Equations (6) and (7) to be equal, Equation (1) can be obtained.

$$\theta = \frac{C_D d}{2} \qquad (8)$$

For a wing of finite aspect ratio, the momentum thickness becomes $C_D b/2$ where b is the span of the wing. As the velocity profile moves downstream, the amplitude (or the mean velocity (U_0)) of the profile decreases, while the width L_0 increases. An estimate of L_0 and U_0 can be obtained at a given distance downstream through the use of an algebraic model as a function of the coefficient of drag of the turbulent generator . This approximation for U_0 and L_0 is shown in Equations (9) and (10), respectively.

$$U_0 = \gamma \frac{U_\infty}{L_0}\theta \qquad (9)$$

$$L_0 = \left(\sqrt{\frac{dx_d}{2\theta}}\right)\theta \qquad (10)$$

where x_d is the distance downstream of the TE of the wing and γ is the empirical factor that was introduced to account for the differences in U_0 between the model and the experimental

data. The U_0 and L_0 values are used to model a velocity profile with a Gaussian distribution seen in the wake of a turbulent generator using the result from Meunier and Spedding [5]:

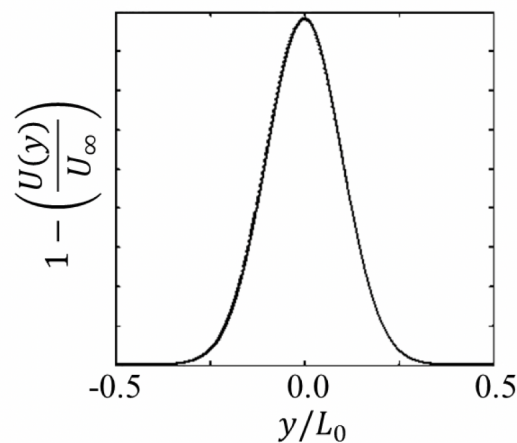$$U(y) = U_0 \exp\left(-\frac{y^2}{2L_0^2} \right) \tag{11}$$

Figure 2. Example of Momentum deficit distribution generated by Equation (12) with $\gamma = 1$.

Although velocity fluctuations are created in three dimensions in turbulent flows, in the present application, streamwise momentum effects are far greater than the cross-stream momentum effects. The effects of cross-stream momentum effects are therefore ignored. Substituting Equations (8)–(10) into Equation (11), the momentum deficit becomes,

$$U(y) = U_\infty \gamma \left(\sqrt{\frac{C_D}{dx_d}} \right) \exp\left(-\frac{2y^2}{C_D dx_d} \right) \tag{12}$$

where U_∞ is the freestream velocity, d is the diameter of the turbulent generator, C_D is the drag coefficient of the turbulent generator, and x is the distance downstream of the trailing edge (TE) of the turbulent generator. An example distribution generated by Equation (12) is shown in Figure 2. Equation (12) can describe the velocity profile (momentum-deficit) behind a turbulent generator based on prior knowledge of its coefficient of drag presuming the underlying assumptions are respected.

2.2. The Reynolds Stress Model

In the wingtip vortex literature, the stable wake zone is defined as the region in the wake where turbulent production is equal to turbulent dissipation. This corresponds to the self-preserved wake referred to in turbulent wake research. Under this condition, the energy from the mean component of the velocity diffuses into the fluctuating velocities (represented in terms of Reynolds stress) which is sustained by the mean shear. This can be quantified in terms of Reynolds stress. Assuming two-dimensional, incompressible flow in the stable wake zone where the velocity gradient as a function of downstream distance is negligible, the Boussinesq approximation simplifies to,

$$u'v' = \nu_T \frac{dU(y)}{dy} \tag{13}$$

where ν_T represents the eddy viscosity. The derivative of the velocity in Equation (13) is found from Equation (11). By taking the derivative of Equation (11), $(dU(y)/dy)$, and then substituting into Equation (13) and simplifying, the Reynolds stress equation becomes,

$$u'v' = A \frac{y}{L_0} \exp\left(-\frac{y^2}{2L_0^2} \right) \tag{14}$$

The amplitude A in Equation (14) is,

$$A = \nu_T U_0 \tag{15}$$

The expression for eddy viscosity shown in Equation (15) is found using the relation,

$$\nu_T = \nu R_l \tag{16}$$

where R_l is the characteristic Reynolds number based on the turbulent length scale and turbulent velocity found at a given downstream distance and is represented by Equation (17).

$$R_l = \frac{(U_0 L_0)}{\nu} \tag{17}$$

Substituting Equations (8)–(10) and (15)–(17) into Equation (14), the Reynolds stress becomes

$$u'v' = (U_\infty)^2 \frac{bC_D}{d\gamma x_d} y \exp\left(-\frac{2y^2}{C_D d x_d}\right) \tag{18}$$

It is interesting to note that the empirical factor γ that appears in Equation (18) changes the amplitude of the distribution, which tunes the model to the specific circumstances of the experiment. As the amplitude of the Reynolds stress distribution is determined by eddy viscosity, as shown in Equation (15), the empirical factor γ can act as a surrogate for eddy viscosity. An example distribution reproduced by Equation (18) is shown in Figure 3 with $\gamma = 1$.
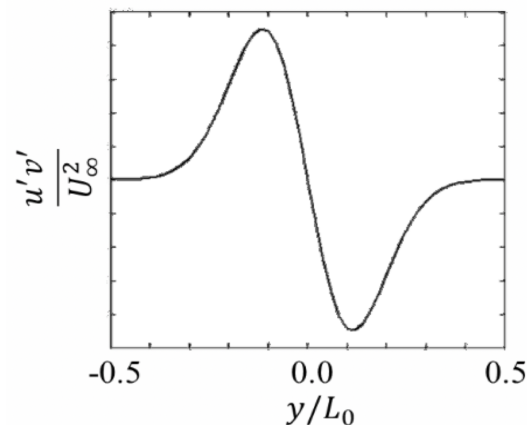

Figure 3. Example of Reynolds stress distribution generated by Equation (18). The distribution resembles the Reynolds stress profile in the wake of a turbulent generator.

The sensitivities of the Reynolds stress model to its various input parameters is shown in Figure 4. The independent axis is the percentage change in the variables such as coefficient of drag, freestream velocity, downstream distance, and thickness to chord ratio of turbulent generator. The dependent axis is the percentage change in the maximum value (peak) of the Reynolds stress distribution. Figure 4a indicates that the model is highly sensitive to the freestream velocity, coefficient of drag, and span. As expected in the stable wake zone, the model shows less sensitivity to the downstream distance. This observation is consistent with the expected physics. From Equation (18), U_∞ and C_D are the variables usually associated with contributing to the Reynolds stress. The relationship between the percentage change in the input parameters and percentage change in the positive peak value is linear except for the diameter (Figure 4b). However, the sensitivity of the Reynolds stress to the diameter is an order of magnitude lower.
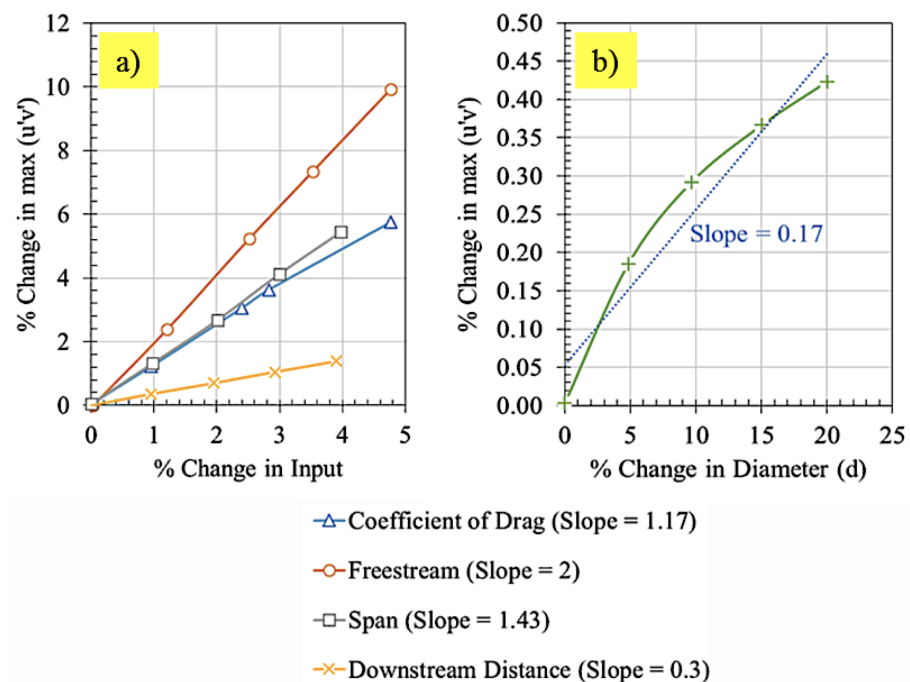
Figure 4. Sensitivity of the Reynolds stress model with (**a**) C_D, U_∞, span and downstream distance, (**b**) diameter.

3. Previous Experimental Work

In the experiments done by Ganci and Altman [6] in the University of Dayton Low Speed Wind Tunnel (UD-LSWT), the authors applied the Reynolds stress model to the Reynolds stress distributions in the wake of a circular cylinder, SD7062 AR 7 wing, and a small remote control (R/C) aircraft. The work was focused on the application of a wake identification technique. However, the empirical factor was not yet identified as part of that work. A sensitivity analysis on streamwise location identified the streamwise bounds of the self-preserved state of the wake. Due to the installation/mounting constraints of the SD7062 AR 7 wing and the remote-control aircraft, insufficient downstream distance was available to reach the stable wake zone before encountering the wind tunnel diffuser. This logistical constraint was overcome by conducting experiments in the United States Air Force Research Labs Horizontal Free Surface Water Tunnel (AFRL/HFWT) on a wall-to-wall SD7003 airfoil (two-dimensional wing) and on an AR 4 flat plate.

4. Experimental Setup

At the time these tests were performed, the free surface water tunnel in AFRL had a 4:1 contraction and 46 cm wide by 61 cm high test section, a freestream velocity range of 3–45 cm/s, and a turbulence intensity of 0.4% at 15 cm/s. The tunnel is fitted with a three degree of freedom motion rig (Figure 5) consisting of a triplet of H2W linear motors, driven by AMC DigiFlex servo-drives controlled by a Galil DMC 4040 4-channel card, with user-selected proportional/integral/derivative (PID) constants for each channel. A photo of the HFWT with the PIV test setup is shown in Figure 6.

Particle Image Velocimetry (PIV) was conducted using a PCO 4000 camera with a 105 mm Nikon lens connected to a LaVision PIV system via a CamLink interface using a single analog to digital converter. The field of view (FOV) of the interrogation region was 120 mm × 80 mm (4.7 in × 3.1 in.) with a final resolution of 34 pixels/mm. A 200 mJ/pulse frequency doubled Nd:YAG laser was used as a light source with the thickness of 1.5 mm. TiO2 with a scattering cross section of 10 microns was used to seed the water tunnel. The between the image pairs were determined to allow particles to travel 8–10 pixels in the CCD array of the camera for better correlation in the free shear layer of the wing (targeting a final 32-pixel interrogation region). Two iterations were used in the post processing.

The first with 64×64 interrogation windows and the second with 32×32 interrogation windows given a final vector resolution of 1 vector/mm.
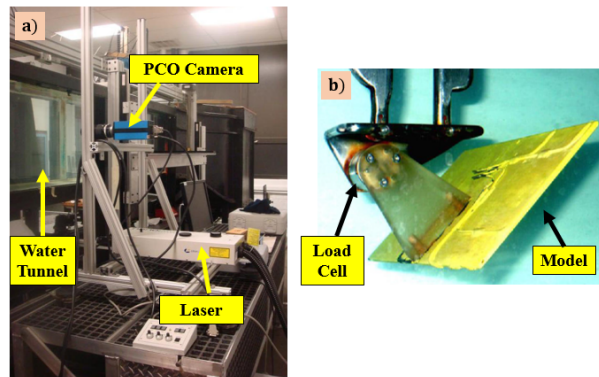

Figure 5. (**a**) PIV Setup in HFWT (**b**) Mounting of model to load cell in HFWT.
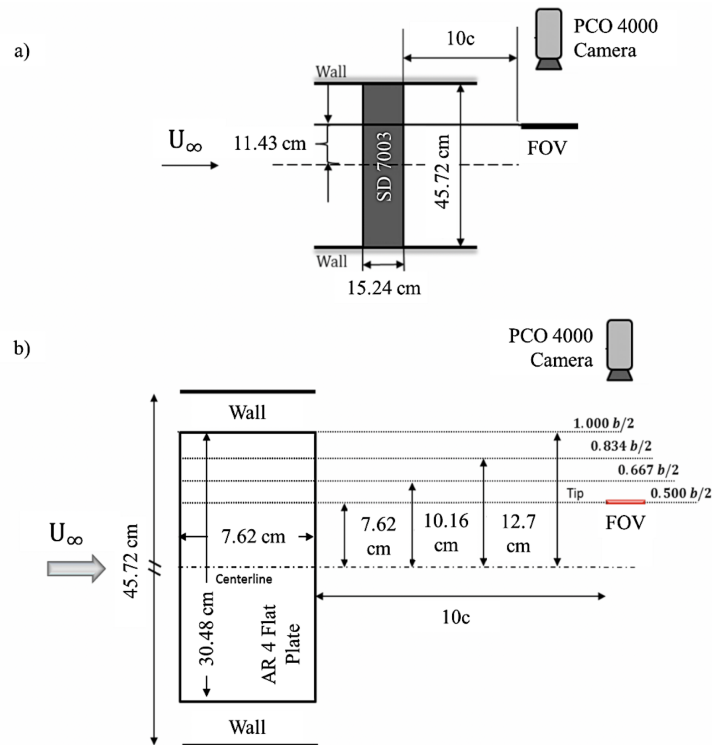

Figure 6. PIV test setup for (**a**) SD7003 and (**b**) AR 4 flat plate (dimensions are not to scale).

4.1. Test Matrix

An overview of the tests conducted in the AFRL-HFWT is shown in Table 1. The mid semispan free shear layer in the wake of the SD7003 wall-to-wall model and different spanwise stations in the wake of an AR 4 flat plate were interrogated.

Table 1. Test matrix of streamwise PIV done at AFRL-HFWT on SD7003 wall-to-wall model and AR 4 flat plate.

Model	$x_d(c)$	α	Interrogation Location (b/2)
SD7003 Wall-to-Wall	6, 8, 10, 20	$2°, 4°, 6°, 8°$	0.5
AR 4 Flat Plate	4	$4°$	0.50, 0.67, 0.83, 1.00

4.2. SD7003 and AR 4 Flat Plate Test Setup

The mid semispan free shear layer wake of the SD7003 wall-to-wall model was interrogated at 2°, 4°, 6°, and 8° angles of attack. The wake of an AR 4 flat plate at an angle of attack of 4° was also interrogated from the mid semispan station to the wingtip in increments of 2.54 cm (1″). In both cases, the PIV field of view was aligned 10 chord lengths downstream of the TE of the wing (Figure 7). The chord length-based Reynolds number was 32,000 and 64,000 for the AR 4 flat plate and SD7003, respectively. The specifications of the water tunnel models are tabulated below (Table 2). A schematic of the test setup for the SD7003 and AR 4 flat plate is shown in Figure 7.

Table 2. Geometry of the models and conditions for experiments conducted at the AFRL/HFWT.

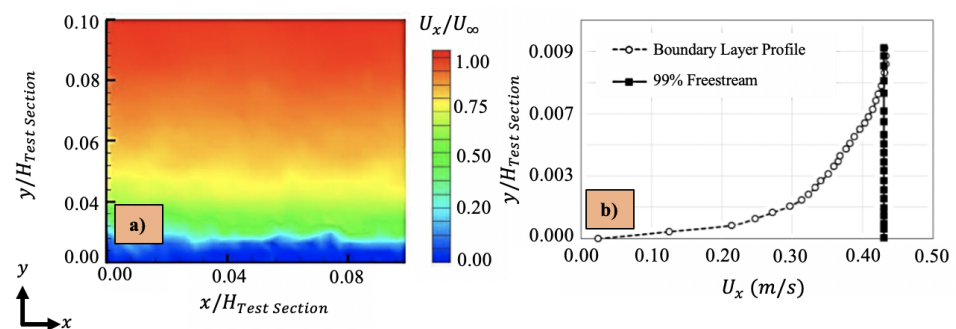| Parameter	AR 4 Flat Plate	SD 7003
Aspect Ratio	4	Wall-to-Wall
Mean Aerodynamic Chord (cm)	7.62	15.24
Wingspan (cm)	30.4 (12″)	45.7
Surface Area (cm^2)	232	697
Reynolds Number	32,000	64,000
Downstream Interrogation Distance (c)	10	10

Figure 7. Boundary layer (**a**) contour and (**b**) profile taken at 8 chord lengths from where the model was supposed to be mounted.

5. SD 7003 Results

The effects of boundary layer growth along the tunnel walls of HFWT was taken into account. Since the HFWT has three solid surfaces and one free surface, the effective test section area is gradually reduced with downstream distance due to the growth of the wall boundary layer, which results in a slight increment in velocity as a function of downstream distance. Figure 7a,b shows the contour and the profile of boundary layer at eight chord lengths from the trailing edge of the model. No model was mounted in the test section for this measurement since the model would bias the results. It was determined that the effect of boundary layer growth on the wake was negligible.

Figure 8 shows the 8° angle of attack SD 7003 wall-to-wall model streamwise velocity component $U(y)$ as a function of y. The image shown in Figure 8 was obtained by averaging 1000 image pairs. There is less than 1% change in the velocity between the free-surface side of the wake and the wall. This slight gradient in the freestream is not the cause of the asymmetry in the Reynolds stress profiles shown in the results below. The asymmetry observed in the Reynolds stress distributions is a unique feature of the free shear layer wake behind a lifting wing. The asymmetry in the Reynolds stress distributions has been observed in wind tunnels with both an open jet and closed test section with no significant measurable a priori gradient in the freestream [6–10].
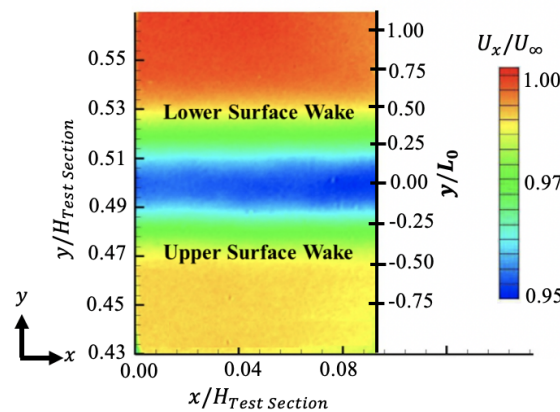
Figure 8. $U(y)$ distribution showing slight gradient (1.0%) from the top (free surface) to the bottom (solid surface) (with wing model in the test section).

The lift and drag coefficient variation for the SD7003 airfoil are shown in Figure 9. The data shown here were extracted from Catalano and Tognaccini [7] for Reynolds numbers similar to those tested in this study. The lift curve for the SD7003 airfoil shows a slight decrease in lift slope from 6° to 8° angles of attack. The lift to drag ratio, however, shows a drastic decrease in aerodynamic efficiency across the same 6° to 8° angles of attack interval. One of the primary objectives of this work is to identify whether or not the macroscopic highest aerodynamic efficiency corresponds to the lowest turbulence in the wake. This analysis is described further in the sections below.
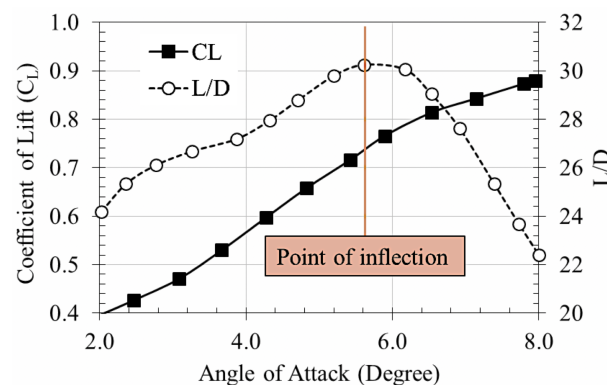

Figure 9. SD7003 airfoil lift curve and L/D variation with angle of attack at Reynolds number 60,000 [7].

5.1. Streamwise Velocity ($U(y)$)

To provide context for correctly applying wake deficit techniques at extraordinarily large distances downstream, it is necessary to provide a brief review of wake interrogation literature. Most wake interrogations are done to determine drag of the turbulent generator since drag force is an order of magnitude less than the lift force. This small magnitude makes it more challenging to determine drag accurately using the same force transducer as that used for lift. Experimental measurements for determining drag through a control volume approach is common wind tunnel practice. In most cases, however, it has only been applied in the near field.

In 1925, Betz [8] modified the integral formulation to consider the presence of wind tunnel walls and reduced the area of integration to the region directly behind the model. Unfortunately, the Betz model did not account for drag resulting from vortices, which is an important aspect of measuring the drag of a finite wing. Maskell [9] furthered Betz's work and developed a wake integral expression for the induced drag. Since then, various improvements to the Betz–Maskell method have been made for experimental measurements, but most of these have been applied to the near wake. The effect of the

location of the downstream survey plane on the results was not investigated by Betz and Maskell.

El-Refaee [10] was among the first to study the sensitivity of drag predictions with respect to downstream distance using a wake deficit technique and found that drag estimations done at three chord lengths downstream (referred as "moderate" downstream distance in [10]) compares better to direct force measurement experimental data than the one chord length downstream case. El-Refaee showed that attenuation of spurious vorticity happens around three chord lengths downstream. Selig and McGranahan [11] performed drag measurements on airfoils at 1.25 chord lengths downstream of the trailing edge of wings assuming that the wake had relaxed to tunnel static pressure at that downstream location. Goett [12] showed that the greatest differences in drag, as measured at one and three chord lengths downstream is approximately 3%. However, Doetsh [13] concluded that sufficient information is not available to warrant the conclusion that the measured drag was independent of the downstream distance. Even though drag measurement is not the intent behind the present research, it is nonetheless evident that, to determine drag through wake deficit measurement, most experimental investigations have been in the near wake. There have been few attempts at applying this technique 10 chord lengths downstream. The results in the current study show that there is another possibility for extracting performance information, this time from the far wake as well.

Figure 10a shows the variation of the freestream normalized velocity $U(y)$ distribution across different angles of attack 10 chord lengths downstream of the TE of the SD7003 airfoil. The 2° case has the highest minimum normalized velocity and the 8° case has the lowest minimum normalized velocity, showing the increased momentum deficit with increase in angle of attack in the range considered here. Intuitively, this is expected due to the coincident increase in the coefficient of drag (Figure 10b), although nowhere in the literature is this found to be documented as far as 10 chord lengths downstream. The coefficient of drag information for the SD7003 was obtained from [7].
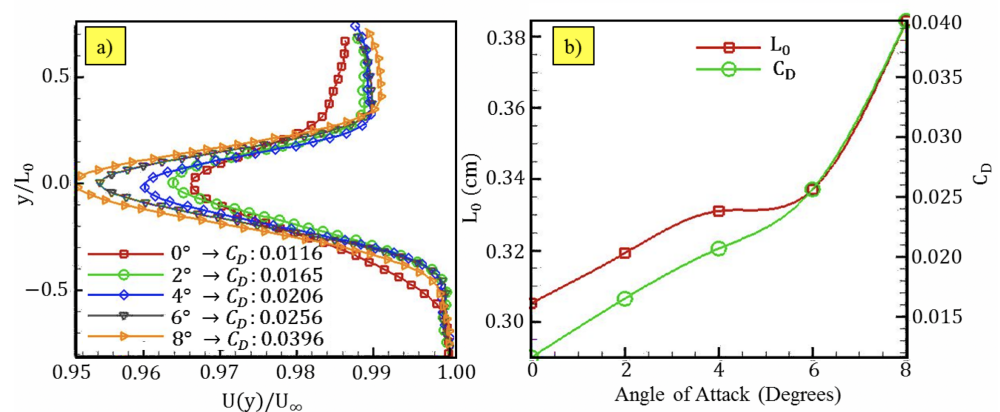

Figure 10. (**a**) Normalized ($U(y)$) variation. (**b**) Variation of coefficient of drag and maximum L_0 with α.

The increment in drag also manifests in the form of higher wake thickness, as seen in Figure 10b. The 8° case has a larger wake half width when compared to the 2° case, and the same trend is seen in the drag coefficient results. A steady increase in wake half width can be seen from 2° to 6° and a steep increase can be seen from 6° to 8° angles of attack. This corresponds to the decreased aerodynamic efficiency seen in Figure 9. This increment in drag and the wake thickness is attributed to the formation of laminar separation bubble in the upper surface of the SD7003 airfoil, as indicated in Radespiel, Windte, and Scholz [14]. A laminar separation bubble is observed on the upper surface of the SD7003 airfoil. The presence and growth of the laminar separation bubble was further studied through XFOIL simulations.

The displacement thickness over the SD7003 was estimated using XFOIL under the experimental conditions. From the simulated results, the laminar separation bubble (repre-

sented by the hump in the displacement thickness results in Figure 11) propagates towards the leading edge (LE) of the wing with increase in angle of attack. The corresponding increase in the trailing edge displacement thickness can also be observed through the high gradient in the displacement thickness (δ) (Figure 11a) and the momentum thickness (θ) (Figure 11b) between 6° and 8°.
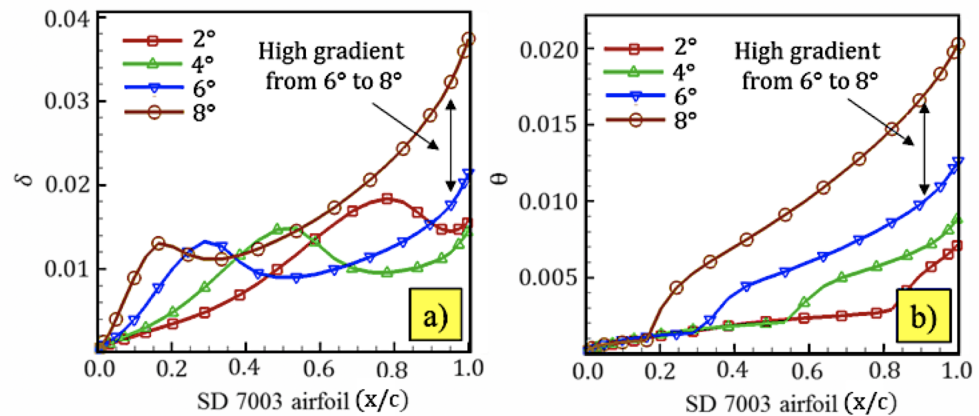

Figure 11. SD7003 upper and lower surface (**a**) displacement thickness (δ) and (**b**) momentum thickness (θ) at different angles of attack.

A steep increase in both the displacement thickness and the momentum thickness from 6° to 8° angles of attack indicates flow separation from the upper surface of the airfoil. The increase in momentum thickness manifests itself as an increase in drag (From Equation (1)) and hence a change in turbulent properties in the flow. The presence of the laminar separation bubble (LSB) is believed to be the cause of the steep increase in the drag and wake half width from 6° to 8° angles of attack in Figure 10b. It is also believed to be the cause of the dramatic decrease in aerodynamic efficiency of the wing from 6° to 8° angles of attack shown in Figure 10. This change in the character of the turbulence exclusively over the upper wing surface is hypothesized to convect into the free shear layer wake and remain stratified despite violent mixing in the wake.

5.2. Reynolds Stress

Figure 12a shows the experimentally obtained normalized Reynolds stress distribution in the wake 10 chord lengths downstream of the SD7003 wall-to-wall model across a range of angles of attack. The Reynolds stresses are normalized by the square of the freestream velocity. All Reynolds stress distributions shown are the result of minimal median filtering and represent averages across roughly 40 sections ($\sim$2.54 cm (1″)) in the center of each velocity vector plot (which is extracted from 1100 image pairs). It is noteworthy that the velocity vector images were corrected for spherical aberrations and freestream [background] turbulence before the profiles were obtained.

The normalized peak Reynolds stresses increase with increase in angle of attack (Figure 12a). The positive peak is generated by the flow over the lower surface of the SD7003 airfoil and the negative peak is generated by the flow over the upper surface of the airfoil. Even 10 chord lengths downstream of the TE, distinct differences between the upper and the lower surface contributions can be observed in the Reynolds stress. As indicated above, this asymmetry is not due to the slight freestream gradient shown in Figure 8 but due to the differences in the nature of turbulence between upper and lower surface boundary layer. Upon closer inspection of the normalized Reynolds stress distributions, the positive peak (lower wing surface) varies almost linearly with angle of attack (Figure 12b).

Similar linearity is not seen in the negative peak (upper wing surface) Reynolds stress variation. The 2° case has lower magnitude than the 4° case, which renders the variation non-linear. This non-linear variation of upper surface associated Reynolds stress in this case is thought to be due to the formation of the laminar separation bubble over the upper

surface of the wing, as shown in Figure 11. As hypothesized in the Introduction, there appears to be a correlation between the far wake turbulence and the on-body aerodynamics. A high gradient from 6° to 8° angles of attack can be seen in the upper surface peak Reynolds stress, which resembles the variation in the aerodynamic efficiency shown in Figure 10.
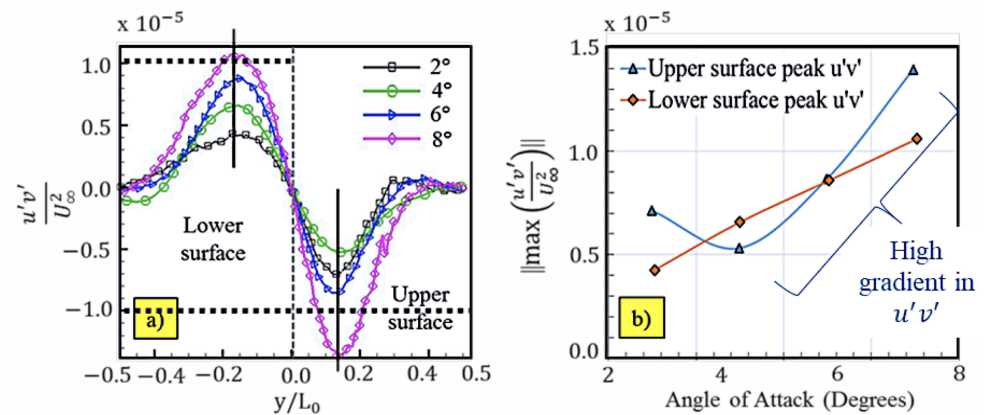

Figure 12. (**a**) Reynolds stress distribution in the wake of SD7003. (**b**) Variation of the peak Reynolds stress with α.

5.3. SD7003 Momentum Deficit Match Using Momentum Deficit Model

The velocity distribution in the wake of an SD7003 wall-to-wall model was matched with the velocity distribution predicted by the momentum deficit model given in Equation (12). For a given angle of attack, all of the variables in the momentum deficit model (Equation (12)) are known except for the empirical factor (γ). The value of was determined at each angle of attack by matching the model to the experimental data. These results are shown for 4° and 6° angles of attack in Figure 13. Although not shown, the 0°, 2°, and 8° angle of attack cases matched similarly well by tuning γ.
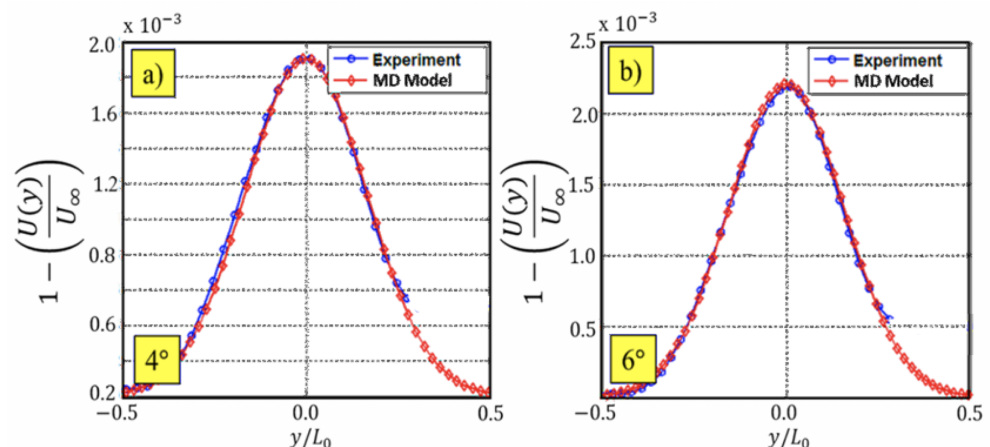

Figure 13. Velocity distribution matches well using momentum deficit (MD) model for SD7003 at (**a**) 4° and (**b**) 6° angles of attack.

The corresponding γ variation across the range of angles of attack tested is shown in Figure 14a. Using the momentum deficit model the γ variation exhibits trends similar to those seen in the aerodynamic efficiency, as highlighted in Figure 14b. A large gradient exists from 6° to 8° angles of attack. The Reynolds stress and momentum deficit profiles shown in Figures 10 and 12 indicate that there might be a relationship between the on-body aerodynamics and turbulence properties in the wake. The variation of γ, however, seems to indicate that the performance information of the wing might also be preserved in the

turbulence characteristics of the free shear layer. To further bolster this hypothesis, the Reynolds stress model was also used to match the Reynolds stress in order to determine if the same trend exists in the γ variation.
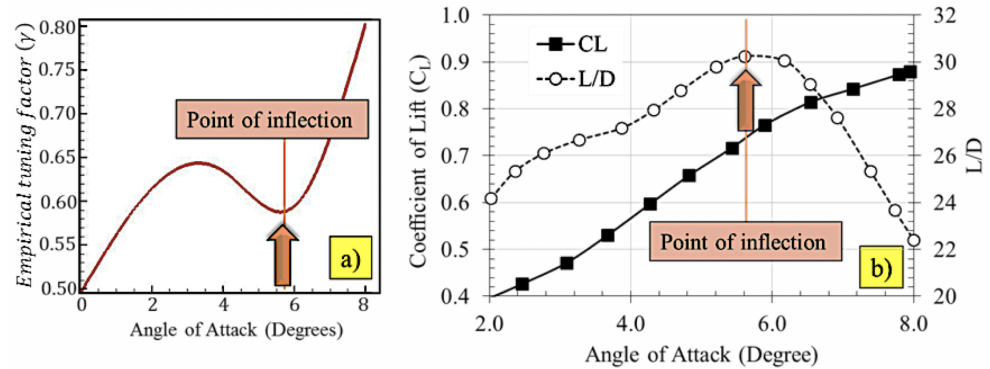

Figure 14. (**a**) Empirical factor (γ) variation found by matching momentum deficit from experiment and MD model. (**b**) L/D profile of the SD 7003 wall-to-wall model.

5.4. Comparison of Experimental SD7003 Wake Reynolds Stress and Reynolds Stress Model

The upper and lower surface Reynolds stress peaks shown in Figure 12a are matched using the Reynolds stress model in Equation (18) for all angles of attack tested. Figure 15 shows the model-matched Reynolds stress distributions for the SD7003 for the 4° and 6° angle of attack cases.

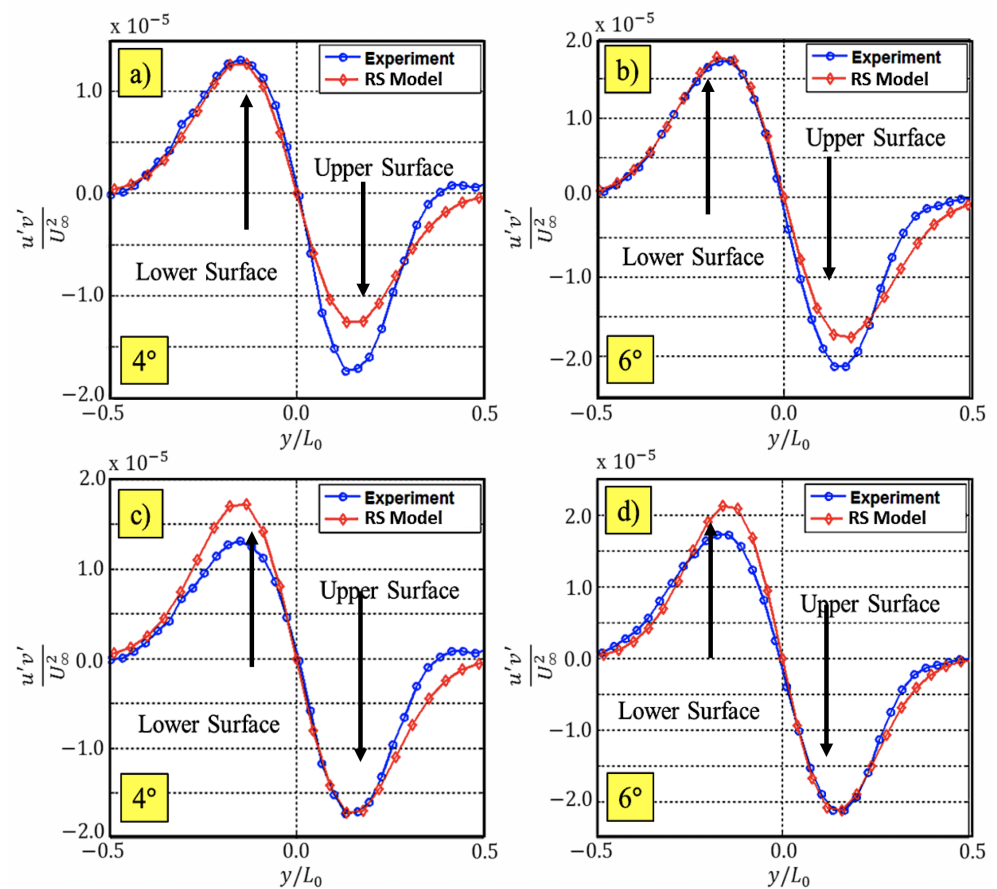**Figure 15.** Comparison of experimental Reynolds stress and the Reynolds stress model shown in Equation (18) for (**a**) 4° and (**b**) 6° lower surface Reynolds stress and (**c**) 4° and (**d**) 6° upper surface Reynolds stress.

The 2° and 8° angle of attack cases were also matched using the model. While matching Reynolds stress distributions, the empirical factor (γ) was changed to match the upper surface peak and the lower surface peak of the Reynolds stress distribution. Figure 15a,b shows the positive peak match of the Reynolds stress distribution, while Figure 15c,d shows the negative peak match of the Reynolds stress distribution. The model in its present form cannot match the positive and negative peaks simultaneously due to the asymmetry in the Reynolds stress distribution. However, the addition of γ to the model provides the flexibility to match the positive and negative peaks separately.

It can be seen in Figure 16 that both the upper surface and lower surface associated Reynolds stress remains comparatively constant from 2° to 6°, and there is an increase in γ from 6° to 8° angles of attack. Once again, this trend matches with the trends seen in Figures 9 and 10b. The trend also resembles the γ variation obtained from the momentum deficit model match shown in Figure 14a. γ changes significantly (though similarly) from 6° to 8° for both the positive and negative peaks. This change in eddy viscosity might be embodied in the change in the empirical factor γ.
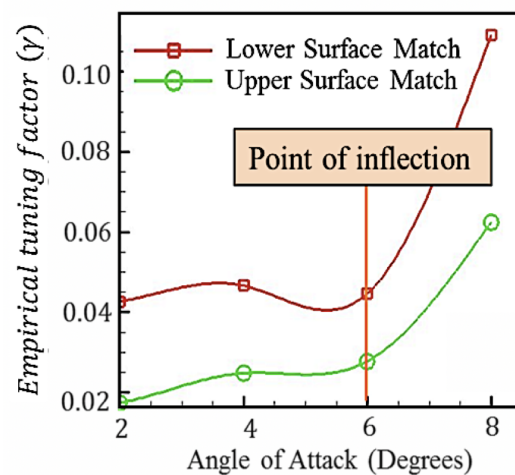

Figure 16. Variation in the empirical factor (γ) in the Reynolds stress model for positive and negative peaks.

5.5. SD7003 RMS Variation

Besides the Reynolds stress variation, the root mean square of the streamwise and cross-stream velocity in the wake is compared against different angles of attack. The RMS of the streamwise and cross-stream velocity are determined by taking the square root of the ensemble average of the square of the fluctuating velocities, as shown in Equations (19) and (20).

$$U_{RMS} = \sqrt{\overline{u'^2}} \tag{19}$$

$$V_{RMS} = \sqrt{\overline{v'^2}} \tag{20}$$

The normalized RMS variations in the wake of the SD7003 wall-to-wall model are shown in Figure 17 for different angles of attack. The bimodal distribution of U_{RMS} in Figure 17a shows a higher deviation in the magnitude of the RMS from 6° to 6° angles of attack. This indicates increased turbulent fluctuations in the streamwise velocity component in the wake. Similar variations are also seen in the V_{RMS}. This variation indicates increased turbulent fluctuations in the cross-stream component in the wake mirroring the on-body momentum and displacement thickness, aerodynamic efficiency, drag coefficient, wake half width, and Reynolds stress variation.

Therefore, one potential conclusion from the results in Figures 14a and 16 is that variations in the aerodynamic efficiency of a 2D wing are preserved in the turbulence

characteristics (Reynolds stress, RMS) and in the mean characteristics (momentum deficit) in the far wake 10 chord lengths downstream of the wing. The consequent logical question is whether or not the results would be the same for a three-dimensional case. An AR 4 flat plate is thus presented next.
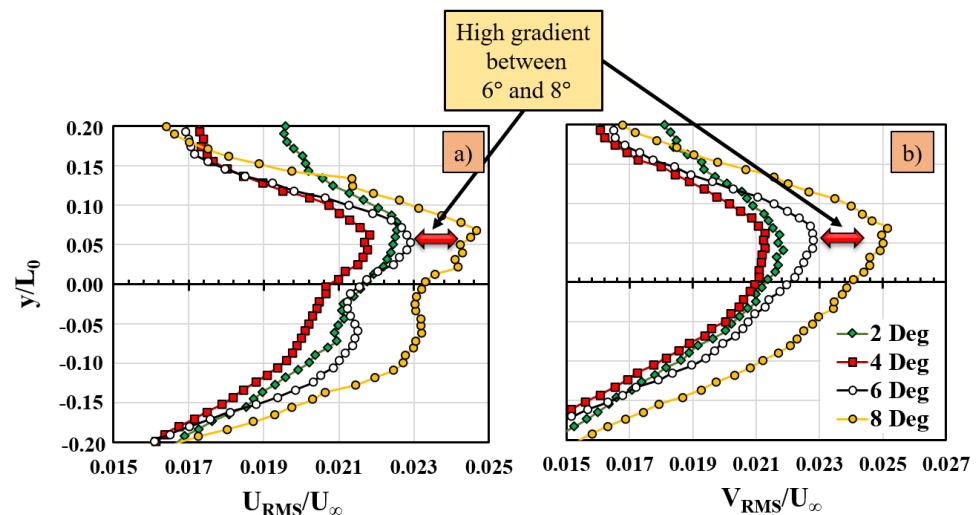

Figure 17. Variation of (**a**) streamwise U velocity and (**b**) cross-stream V velocity RMS in the wake of SD7003 wall-to-wall model. A large increase in magnitude of RMS can be seen from 6° to 8° angles of attack.

6. AR 4 Flat Plate Results

The wake of the AR 4 flat plate is interrogated 10 chord lengths downstream at several spanwise locations at a fixed angle of attack of 4°.

6.1. Streamwise Velocity Variation $U(y)$

Figure 18 shows the normalized U-velocity as a function of spanwise distance at 10 chord lengths downstream. In Figure 18, the mean velocity U_0 decreases with distance from the mid semispan to the wingtip. There is a slight decrease in the peak $U(y)$ velocity (U_0) from the $0.667b/2$ spanwise station to the $0.834b/2$ spanwise station. There is a significant drop in the peak $U(y)$ velocity in the outboard wingtip vortex station ($1.000b/2$). This trend indicates that the local drag is higher at the mid semispan and lower at the wingtip similar to the nature of lift and drag distribution in a span loaded wing. The momentum deficit at the tip station shows the interference of the free shear layer with the wingtip vortex. Even at 10 chord lengths downstream, the wingtip vortex remains sufficiently stratified to be distinctly identified. This interaction is also seen clearly in the Reynolds stress distribution in the next section. The interaction of the wingtip vortex with the free shear layer was investigated in much greater detail by Gunasekaran and Altman [15].
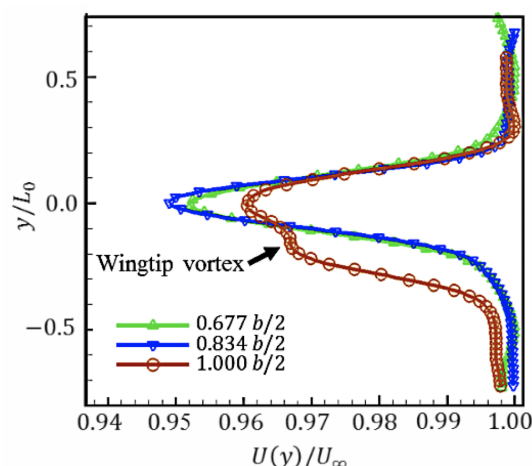
Figure 18. Normalized U-velocity distribution at 10 chord lengths downstream from the TE of the wing at different spanwise stations.

6.2. Reynolds Stress Variation

Figure 19a shows the normalized Reynolds stress distributions at different spanwise stations in the wake at 10 chord lengths downstream from the trailing edge of the wing. The mid-semi span spanwise station has the highest peak Reynolds stress magnitude and the wingtip spanwise station has the lowest peak Reynolds stress magnitude. This trend is similar to what is observed in the peak $U(y)$ velocity shown in Figure 20. Presuming a roughly elliptical distribution of lift over the wing, this result is once again in alignment with expectations. The effect of the wingtip vortex on the Reynolds stress distribution is seen between the positive and the negative peaks of the Reynolds stress distribution at the wingtip spanwise station. To substantiate the hypothesis of the presence of the wingtip vortex in the Reynolds stress distribution at the wingtip, the Reynolds stress of the wingtip vortex in Figure 19a was compared with the wingtip vortex Reynolds stress behavior documented by Phillips and Graham [16], which confirmed the shape of the wingtip vortex Reynolds stress distribution at the wingtip.

Figure 19a shows that the wingtip vortex is sandwiched between the shear layers emanating from the upper and lower surface. However, the general variation of Reynolds stress is not affected by the presence of the wingtip vortex. This was confirmed by the results in Figure 19b, where the wingtip vortex Reynolds stress was cropped from the wingtip Reynolds stress profile, and the resulting Reynolds stress profile resembles the Reynolds stress profiles of the inboard cases.
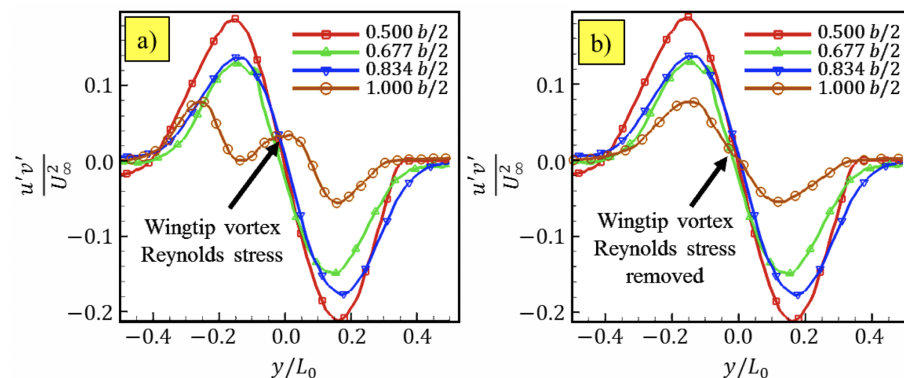

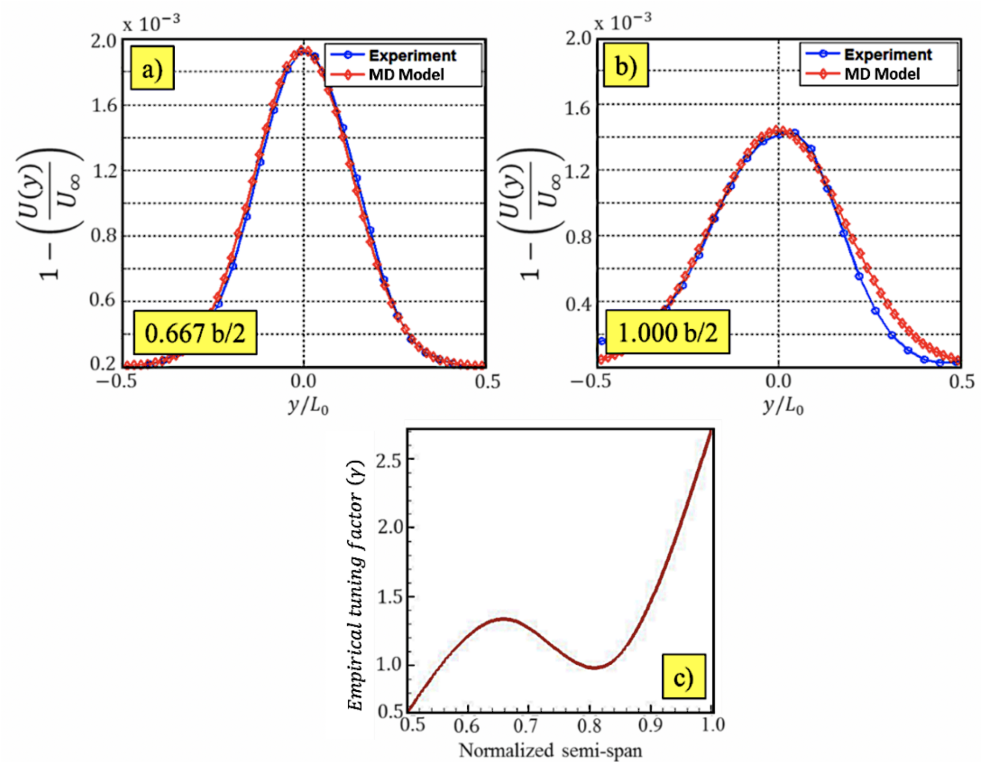**Figure 19.** Flat plate wake Reynolds stress distributions (**a**) with wingtip vortex and (**b**) without wingtip vortex.

Figure 20. Comparison of Momentum Deficit model and experimental data at (**a**) 0.677b/2 and (**b**) 1.000 b/2 and (**c**) the empirical factor γ variation.

It is hypothesized that the changes in the peak magnitude of the Reynolds stress distribution and changes in the peak U_0 in the velocity distribution are due to the variation of lift as a function of span along the wing. These observations, along with the observations made in the wake of SD7003 wall-to-wall model, demonstrate that there is a significant relationship between the on-body aerodynamics and the far wake. It also shows that the variation in on-body aerodynamics is preserved well into the far wake. The results of Phillips and Graham [16] do not extend beyond the boundary of the wingtip vortex outer core and as such do not elucidate any interaction with the free shear layer generated by the upper and lower wing surface boundary layers meeting at the TE. Inspecting Figure 21, it is highly probable that the free shear layer has a significant effect on the rollup process of the wingtip vortex in the near wake. This interaction was studied further by Gunasekaran and Altman [15].

6.3. AR 4 Flat Plate Momentum Deficit Match Using Momentum Deficit Model

The momentum deficit model shown in Equation (12) was used to match the experimental momentum deficit distribution shown in Figure 18. Figure 20 shows the match between the model and the experiment for the 0.667 b/2 and wingtip 1.000 b/2 spanwise stations. The clear stratification of the wingtip vortex at the wingtip station enabled the removal of the wingtip vortex contribution at the wingtip station to facilitate the match. The empirical factor (γ) is adjusted to match the mean velocity U_0 and the distribution.

The spanwise variation of γ shown in Figure 20c demonstrates an increase from the mid semispan station to the wingtip station. This could be an indication of the local change in the magnitude of turbulence. This is expected because, at the wingtip, the wingtip vortex is expected to cause greater flow disruption than at any other spanwise location.

6.4. Comparison of Experimental SD7003 Wake Reynolds Stress and Reynolds Stress Model

The Reynolds stress peaks corresponding to the upper and lower surface of the wing shown in Figure 19b are compared with the Reynolds stress model shown in Equation (18)

for each spanwise stations. Figure 21 shows the model-matched Reynolds stress distributions for the AR 4 flat plate at the 0.667 b/2 spanwise station and at the wingtip vortex spanwise station. The spanwise variation shown in Figure 21e demonstrates an increase from the mid semispan to the wingtip in line with the results from the momentum deficit model (Figure 20c).

Although γ is an empirical factor, the trend of its variation shown in both the SD7003 wall-to-wall model and the AR 4 flat plate cases seem to mimic the expected physical characteristics of the flow in each case. It also provides a way to extract the performance information of the turbulent generator at relatively long distances downstream of the trailing edge which is quite surprising. Therefore, its inclusion in the momentum deficit model and the Reynolds stress model proved to be valuable.
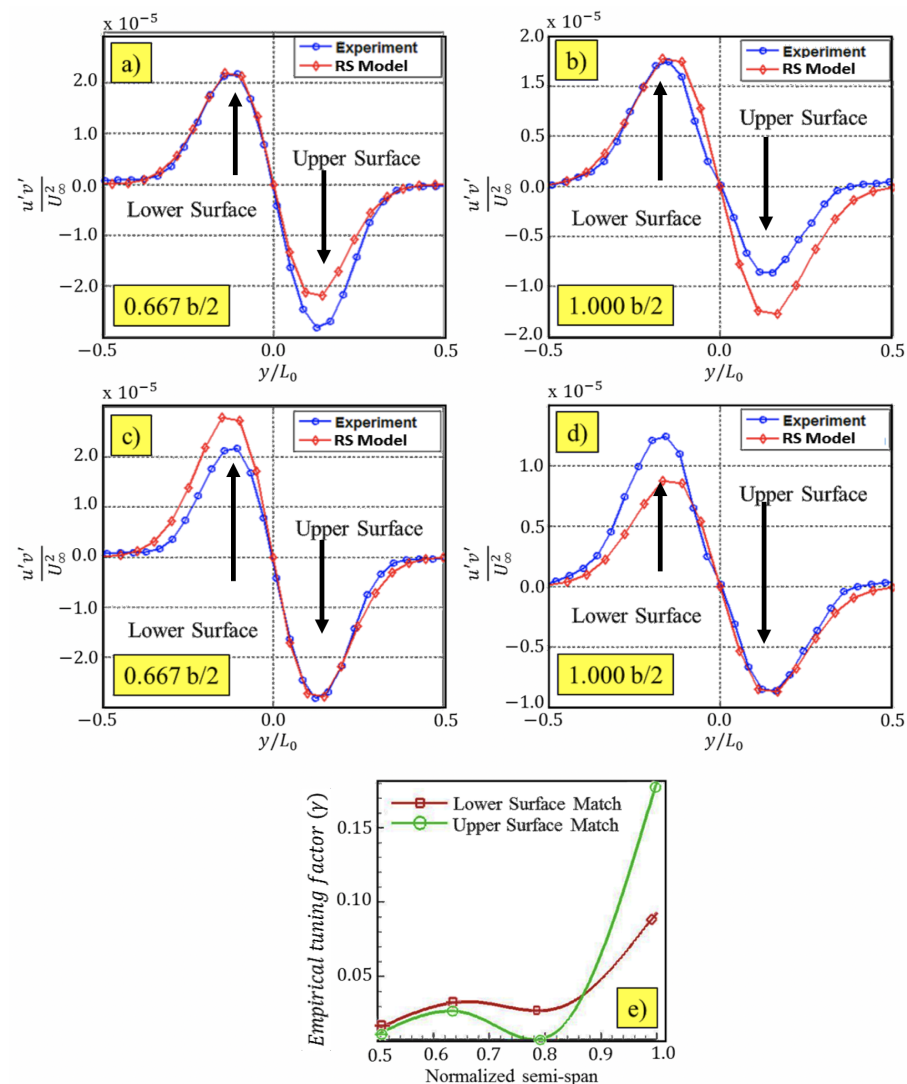

Figure 21. Comparison of RS model with experimental data for upper (**a**,**b**) and lower surface (**c**,**d**) Reynolds stress. (**e**) Variation in the empirical factor γ in the Reynolds stress model for positive and negative peaks.

6.5. RMS Variation in the Wake of AR 4 Flat Plate

Similar to the SD7003 wall-to-wall model case, the root mean square of the streamwise and cross-stream velocities was determined in the wake of AR 4 flat plate using Equations (19) and (20) and is shown in Figure 22 for three different spanwise locations. The U_{RMS} shows a bimodal distribution, indicating the upper surface RMS is higher when compared to the lower surface at different spanwise stations. Because of the increased

wake width at the wingtip, the net turbulent fluctuations at the wingtip is greater when compared to the inboard spanwise stations. This can be represented by determining the area under the RMS curves using trapezoidal integration. The variation of the net U_{RMS} and V_{RMS} is shown in Figure 23 as a function normalized spanwise station. On approaching the wingtip, the total RMS in the wake increases. This trend is seen in the variation of empirical factor γ in Figures 20c and 21e as well.
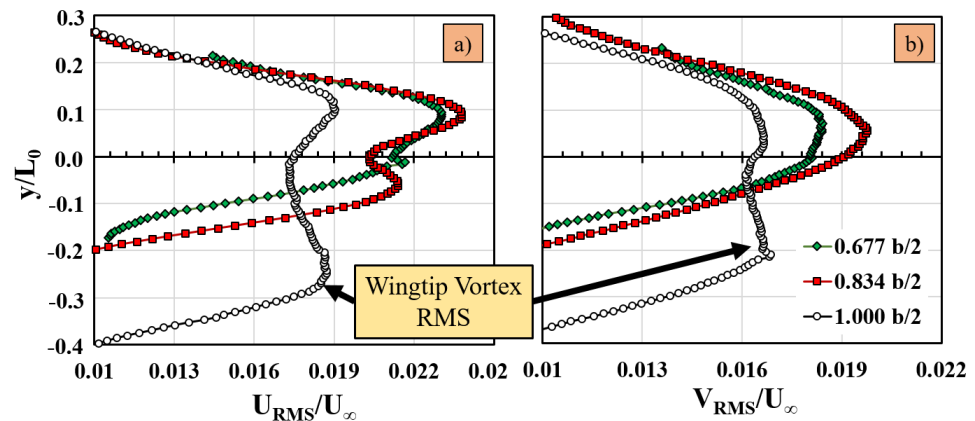

Figure 22. Variation of (**a**) streamwise U velocity and (**b**) cross-stream V velocity RMS in the wake of AR 4 flat plate at different spanwise stations.
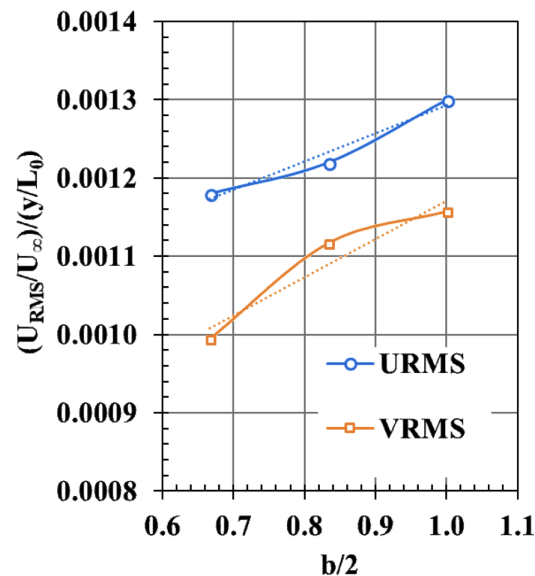

Figure 23. Variation of net RMS as a function spanwise location. The net RMS in the wake increases on approaching the wingtip.

Therefore, one potential conclusion from the results in Figures 20–22 is that even spanwise variations of on-body flow dynamics is preserved 10 chord lengths downstream in the mean (momentum deficit) and fluctuating components (Reynolds stress and RMS) of the wake. The similarity between the wake properties and the empirical factor shows that can be used as a potential indicator of turbulence levels in the flow.

7. Conclusions

Two main conclusions can be drawn from the work presented:

1. A surprising correlation between the aerodynamic efficiency/on-body flow characteristics and the mean and turbulent characteristics of the wake 10 chord lengths

downstream of the wing was found independent of the wing dimensionality (2D or 3D). Despite the violent mixing of the wake, the performance information of the wing is preserved in the wake even after 10 chord lengths downstream. Therefore, the wake is not only unique as discovered by Wygnanski et al. [8], but it also contains detailed information as far as 10 chord lengths downstream of the wing that can be used to reveal the performance information of the wing. This result was concluded from the correlation between the drag coefficient/aerodynamic efficiency, momentum, displacement thickness of the SD7003 wall-to-wall model and the wake half-width, momentum deficit, peak Reynolds stress, streamwise, and cross-stream RMS profiles of the wake at 10 chord lengths downstream. All of these profiles indicated a high gradient from 6° to 8° angles of attack.

2.　The inclusion of the empirical factor γ gave the capability for the momentum deficit and Reynolds stress models to match with the experimental data, especially for modeling wake profiles with similar drag coefficients such as spanwise momentum and Reynolds stress profiles. Even though γ is an empirical factor, its variation with angle of attack resembles the variation of turbulence levels, which indicates that it could be considered as a surrogate for eddy viscosity. This result was concluded from the correlation between the spanwise variation of γ found from the momentum deficit and Reynolds stress models and the streamwise and cross-stream variation of RMS in the wake of the AR 4 flat plate.

While these two conclusions have implications on wake detection and energy harvesting, the robustness of the Reynolds stress model needs to be improved to match the asymmetric distribution of the profiles through physical parameters. To benefit energy harvesting application, and provided the experimental challenges can be overcome, a direct two point spatial and temporal correlation between the near wake and a far wake will yield greater insight into the length scales which influences the forcing function.

References

1.　Wygnanski, I.; Champagne, F.; Marasli, B. On the large-scale structures in two-dimensional, small-deficit, turbulent wakes. *J. Fluid Mech.* **1986**, *168*, 31–71. [CrossRef]
2.　Townsend, A.A. *The Structure of Turbulent Shear Flow*; Cambridge University Press: Cambridge, UK, 1980.
3.　George, W.K. The self-preservation of turbulent flows and its relation to initial conditions and coherent structures. In *Advance in Turbulence*; Hemisphere Publishing Corporation: London, UK, 1989; pp. 39–73.
4.　George, W.K.; Gibson, M.M. The self-preservation of homogeneous shear flow turbulence. *Exp. Fluids* **1992**, *13*, 229–238. [CrossRef]
5.　Meunier, P.; Spedding, G. Stratified propelled wakes. *J. Fluid Mech.* **2006**, *552*, 229–256. [CrossRef]
6.　Ganci, G.; Altman, A.; Rodewald, J. Identification of Aircraft by their Unique Turbulent Wake Signature: Experimental Validation. In Proceedings of the 50th AIAA Aerospace Sciences Meeting including the New Horizons Forum and Aerospace Exposition, Nashville, TN, USA, 9–12 January 2012; p. 66. [CrossRef]
7.　Catalano, P.; Tognaccini, R. Large eddy simulations of the flow around the SD7003 airfoil. In Proceedings of the AIMETA Conference, Bologna, Italy, 12–15 September 2011.
8.　Betz, A. Bin Verfahren zur Direkten Ermittlung des Profilwiderstandes. *ZFM* **1925**, *16*, 42–44.

9. Maskell, E.C. *Progress towards a Method for the Measurement of the Components of the Drag of a Wing of Finite Span*; Royal Aircraft Establishment: Farnborough, UK, 1972.
10. El-Refaee, M.M. Calculation of all drag components for 3-D bodies in wind tunnel flows. A boundary element-wake approach. *Appl. Sci. Res.* **1995**, *55*, 119–139. [CrossRef]
11. Selig, M.S.; McGranahan, B.D. Wind tunnel aerodynamic tests of six airfoils for use on small wind turbines. *J. Sol. Energy Eng.* **2004**, *126*, 986–1001. [CrossRef]
12. Goett, H.J. *Experimental Investigation of the Momentum Method for Determining Profile Drag*; NACA Report No: 660; US Government Printing Office: Washington, DC, USA, 1939.
13. Doetsch, H. Profilwiderstandsmessungen im grossen Windkanal der DVL. *Luftfahrtforsch. Bd* **1937**, *14*, 173–178.
14. Radespiel, R.; Windte, J.; Scholz, U. Numerical and experimental flow analysis of moving airfoils with laminar separation bubbles. *AIAA J.* **2007**, *45*, 1346–1356. [CrossRef]
15. Gunasekaran, S.; Aaron A. Is There a Relationship Between the Wingtip Vortex and the Shear Layer? In Proceedings of the 54th AIAA Aerospace Sciences Meeting, San Diego, CA, USA, 4–6 January 2016; p. 1068. [CrossRef]
16. Phillips, W.R.C.; Graham, J.A.H. Reynolds-stress measurements in a turbulent trailing vortex. *J. Fluid Mech.* **1984**, *147*, 353–371. [CrossRef]